

Radio polarimetry of compact steep spectrum sources at sub-arcsecond resolution

F. Mantovani^{1,2}, A. Rossetti¹, W. Junor³, D.J. Saikia^{4,5}, and C.J. Salter⁶

¹ Istituto di Radioastronomia – INAF, Via Gobetti 101, I–40129, Bologna, Italy

² Max-Planck-Institut für Radioastronomie, Auf dem Hügel 69, D-53121 Bonn, Germany

³ Los Alamos National Laboratory, Los Alamos, NM 87545, USA

⁴ Cotton College State University, Panbazar, Guwahati 781 001, India

⁵ National Centre for Radio Astrophysics, TIFR, Post Bag 3, Ganeshkhind, Pune 411 007, India

⁶ Arecibo Observatory, HC3 Box 53995, Arecibo, Puerto Rico 00612

Received September 30, 2018; accepted ???

ABSTRACT

Aims. We report new Very Large Array polarimetric observations of Compact Steep-Spectrum (CSS) sources at 8.4, 15, and 23 GHz.

Methods. Using multi-frequency VLA observations we have derived sub-arcsecond resolution images of the total intensity, polarisation, and rotation measure (RM) distributions.

Results. We present multi-frequency VLA polarisation observations of CSS sources. About half of the sources are point-like even at the resolution of $\sim 0.1 \times 0.1$ arcseconds. The remaining sources have double or triple structure. Low values for the percentage of polarised emission in CSS sources is confirmed. On the average, quasars are more polarised than galaxies. A wide range of RM values have been measured. There are clear indications of very large RMs up to $\approx 5585 \text{ rad m}^{-2}$. CSS galaxies are characterized by RM values that are larger than CSS quasars. The majority of the objects show very large values of RM.

Conclusions. The available data on sub-arcsecond-scale rest-frame RM estimates for CSS sources show that these have a wide range of values extending up to $\sim 36000 \text{ rad m}^{-2}$. RM estimates indicate an overall density of the magneto-ionic medium larger than classical radio sources.

Key words. polarisation – galaxies: quasars: general – galaxies: jets – radio continuum: galaxies

1. Introduction

The number of Compact Steep-Spectrum (CSS) sources with detailed polarimetric information available at sub-arcsecond resolution is still small. We have conducted a series of polarimetric observations of CSS sources using the Very Large Array (VLA).

CSS objects are *young* radio sources, with ages $< 10^{3-5} \text{ yr}$ (Fanti et al. 1990). They have linear sizes $\leq 20 \text{ kpc}$ ¹ and steep high-frequency radio spectra ($\alpha > 0.5$; $S_\nu \propto \nu^{-\alpha}$). Being sub-galactic in size, CSS sources reside within their host galaxies. Therefore, Faraday rotation effects are to be expected when their polarised synchrotron emission is observed through the magneto-ionic interstellar medium (ISM) of the host galaxy. The comparison of polarised emission over a range of wavelengths is an important diagnostic of the physical conditions within and around these compact radio sources.

Existing sub-arcsec polarimetry has provided evidence in favour of the interaction of components of CSSs with dense gas clouds, (for example, see Junor et al. 1999).

Aiming at a deeper understanding of the CSS source phenomenon, with the VLA² A-Array we observed an “incomplete” sample of 29 sources selected from the list of Dallacasa (1990). The adopted selection criteria were: i) total flux density at 5 GHz $> 1 \text{ Jy}$, ii) declination $> -20^\circ$, and iii) lack of observations at sub-arcsecond resolution (at the time of source selection).

In this paper, we report multi-frequency VLA polarisation observations of our CSS sample at 8.1, 8.5, 15 and 23 GHz.

In Section 2 we summarise the observations and data processing. Section 3 describes the new information obtained on the structural and polarisation properties. Discussion and conclusions are presented in Sections 4 and 5 respectively.

2. Observations and data reduction

Polarimetric observations of our sample of 29 CSS sources were made at 8, 15 and 23 GHz on August 6th, 1991 using the VLA in A-array. The observations were scheduled in “bracket” mode, i.e. calibrator–source–calibrator, to obtain the best possible phase correction. Despite this, almost

Send offprint requests to: Franco Mantovani
e-mail: fmantovani@ira.inaf.it

¹ $H_0 = 71 \text{ km s}^{-1} \text{ Mpc}^{-1}$, $\Omega_m = 0.27$, $\Omega_{vac} = 0.73$

² The National Radio Astronomy Observatory is a facility of the National Science Foundation operated under cooperative agreement by Associated Universities, Inc.

half of the data acquired at 23 GHz could not be imaged due to poor weather conditions. The data were recorded in both circular polarisations, and calibrated in the standard way using AIPS procedures. The sources 2200+420 (BL Lac) and 0923+392 were observed regularly throughout the observing period to allow for parallactic angle corrections. Calibration of the Electric Vector Position Angle (EVPA) was performed by observing the source 1328+307 (3C286) assuming an EVPA of 33° for it at all frequencies. An iterative procedure was carried out using the IMAGR and CALIB programmes to self-calibrate the parallel-hand (LL or RR) fringes. The complex gain corrections derived in this way were also applied to the cross-hand (RL or LR) fringes. Images in Stokes parameters I, Q, and U were produced. Images of the polarised flux density $P=(Q^2+U^2)^{0.5}$ and EVPA, $\chi = 0.5 \times \tan^{-1}(U/Q)$, were then generated from the Q and U images. The data acquired with the 8 GHz receiver were separately imaged for the two IFs, namely IF1 at 8085 MHz and IF2 at 8485 MHz, each having a bandwidth of 50 MHz. When considered together, observations at these two frequencies are designated “X-band” in the text.

3. Results

3.1. Images

The full-resolution images are available on the web site <http://db.ira.inaf.it/aj206-fm/>.

In practice, half of the sources (15) are point-like at our resolution. However, two of these are slightly extended on one side. Seven others show double structure, and six more are triples. One further source is classified as complex. Examples of sources classified as above are presented in Fig. 1. This morphological description follows that of (Spencer et al. 1991). The vectors representing the electric vector of linearly polarised intensity are overlaid on the total-intensity contours.

3.2. Polarised emission

The great majority of the sample sources show evidence of polarised emission. However, generally, they are only weakly polarised. Three sources, namely 0531+194, 0941–080, and 1311+678, show no polarised emission above the detection limits at any of the frequencies observed. The median percentage polarisations measured are summarized in Table 1. The polarisation percentage integrated over complete sources decreases from high to low frequencies, with quasars more polarised than galaxies. It could be noted that there are sources in which the polarisation percentage of individual components are higher than the polarisation percentage integrated over the complete source. This is due to averaging with a range of EVPAs.

The classification of source structures, together with percentage polarised emissions derived by integrating the total-intensity and the polarised-intensity emissions over the total extent of each source, and the depolarisation indices DP, defined as the ratio of the percentages of polarised emission at the lower to the higher frequencies, are reported in Table 2. In Tables 3–6, the polarisation parameters derived for the distinct components of each source at each observing frequency are reported. When more than one PA is listed in the Tables these refer to regions with different

EVPAs. Further information may be obtained from the on-line images (<http://db.ira.inaf.it/aj206-fm/>).

Fractional polarisations, depolarisation indices, and Rotation Measure values for the individual components of each source are reported in Table 7. The Rotation Measure is defined as $RM = \Delta\chi/\Delta(\lambda^2)$ in $rad\ m^{-2}$ where χ is the PA at wavelength λ , allowing for $n\pi$ with n an integer, in the individual PAs to get the best fit. When three frequencies are available, the ambiguity implied by the integer n can be resolved. The RMs are estimated by fitting the points with a linear least-squares fit. The Rotation Measure in the source rest frame is defined as $RM_{rf} = RM \times (1+z)^2$.

We note that polarimetric parameters are derived from images at the full resolution achieved at the various frequencies. The χ values are those associated with the polarised emission peaks. The errors associated with the χ values used in the $\chi - \lambda^2$ plots are calculated considering the dispersion of χ values in boxes of 5×5 pixels around the positions of maximum polarised emission.

RM plots are also available at the web site <http://db.ira.inaf.it/aj206-fm/>. Examples of RM plots are presented in Fig. 2.

3.3. Comments on individual sources

Some of the CSS sources presented here have been included in other sub-arcsecond resolution observations. Parameters from those studies, and in particular the χ values, have been extracted when appropriate.

0023–263 (OB238) – This source have been observed at the S/X bands using VLBI by Tzioumis et al. (2002) with the SHEVE array. We confirm the double source structure of the source seen at both frequencies.

0114–211, (OC224) – This source was observed with the VLA A-array at 5, 8.4, and 15 GHz by Mantovani et al. (1994) who reported a triple structure. Polarised emission was detected only for the western component “c”. The rest-frame RM was calculated in that paper assuming a conventional value of $z=0.5$. With the present 23.2 GHz observations we detect total intensity and polarised emission only from component “c”. Here we have used a redshift of 1.41 ± 0.05 (McCarthy et al. 1996) for estimating the rest-frame RM.

0116+319 (4C31.04) – This source was observed by van Breugel et al. (1984) at 15 GHz with the VLA. They detected no polarised emission above their detection limit of 1.5% of the flux density of 1226 ± 16 mJy, which is a factor of ~ 1.6 higher than the flux density we find at the same frequency.

0127+233 (3C43) – The subject of many investigations, 3C43 shows a peculiar structure characterized by a sharp bend of more than 90° in the jet. Polarised emission has been reported by van Breugel et al. (1992), Akujor & Garrington (1995), Sanghera et al. (1995), Lüdke et al. (1998) and Cotton et al. (2003c) at sub-arcsecond resolution. The EVPA in all these images made from data taken at different frequencies, is perpendicular to the jet axis, nicely following the bend in the jet. Small values of the RM are found along the jet region, while a high value of RM is measured for the northern component. VLBI observations were reported by Nan et al. (1991), Spencer et al. (1991), and Fanti et al. (2002). Polarimetric VLBI observations were performed by Mantovani et al. (2003) at 8.4 GHz. These

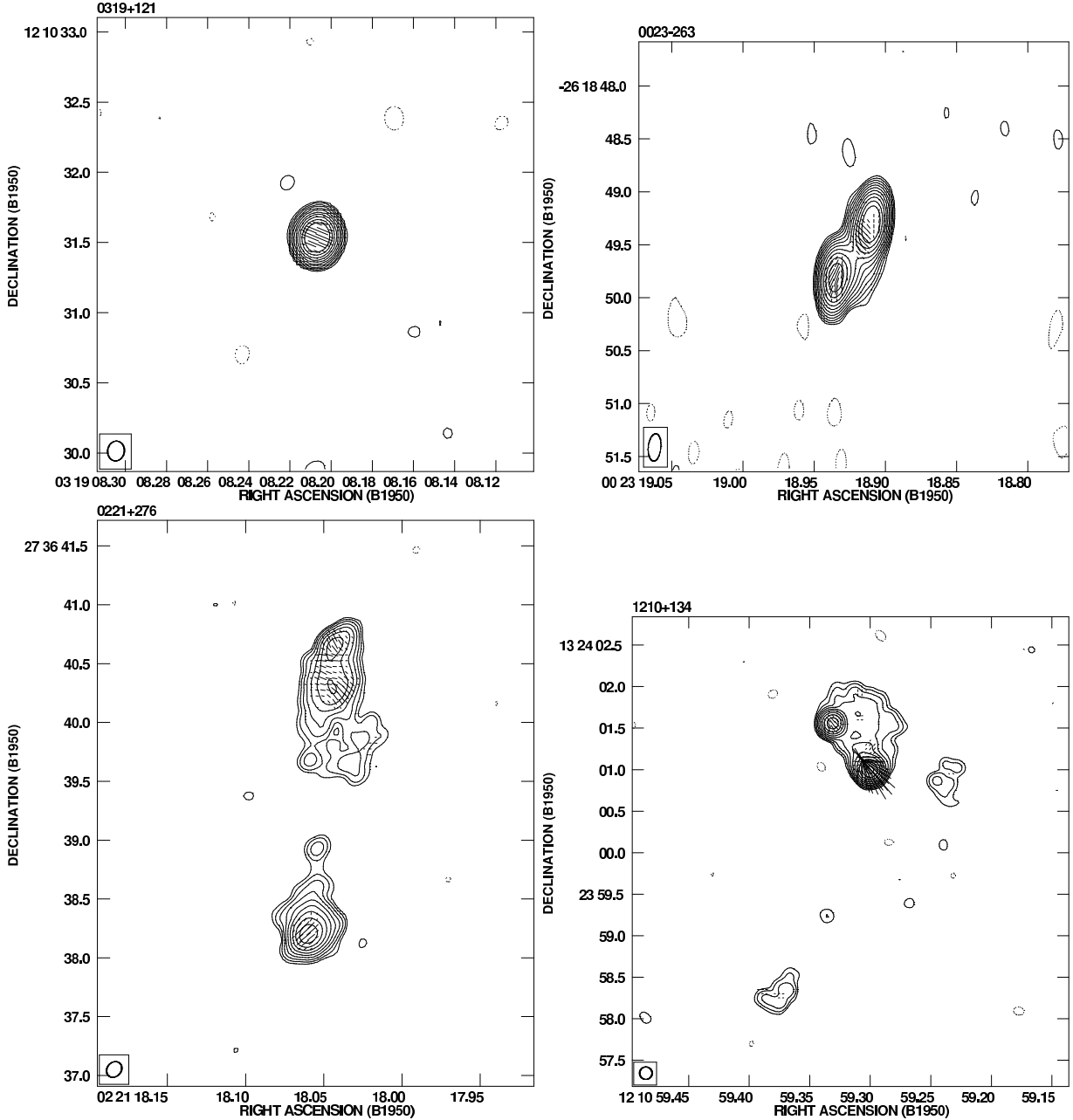


Fig. 1. The total-intensity images of a point-like source (0319+121), a double source (0023–263), a triple source (0221+276), and a complex source (1210+134) at 14885 MHz. The peak flux density is 926.8 mJy/beam, 635.8 mJy/beam, 96.8 mJy/beam, 161.3 mJy/beam, respectively. Contours are $-1, 1, 2, 4, 8, 16, 32, 64, 128, 256, 512, 1024$ mJy/beam. An electric vector length of 1 arcsecond = 200 mJy/beam for 0319+121, and 20 mJy/beam for others.

authors detected polarised emission along the jet with polarisation percentages up to 12%. However, no polarisation was detected from the region of the core. A similar result was obtained at 1.6 GHz by Cotton et al. (2003b). Both articles report a large RM near the bend in the jet.

0221+276 (3C67) – This source shows a triple structure from our 15 GHz observations, as did MERLIN observations at 5 GHz by Sanghera et al. (1995). Because of its almost-flat spectrum, we confirm that the central weak component close to the southern lobe is the core of the source, as suggested by Sanghera et al. (1995) and Lüdke et al. (1998). Of the two lobes, that to the north is strongly polarised at the frequencies we observed. The area with the highest polarised emission shows RMs of up to 1620 rad

m^{-2} in the source rest frame. The southern lobe is 2% polarised at 15 GHz, and depolarises quickly towards lower frequencies. Polarised emission from this component is only marginally detected by our X-band observations. The RM value (~ 3000 rad m^{-2} in the source rest-frame) calculated for this component is rather uncertain.

0223+341 (4C34.07) – The images at 15 and 23.2 GHz reveal a triple structure. The central component is unpolarised and has an almost flat spectrum between the two frequencies. In contrast, both lobes are polarised. However, the less-polarised northern component shows depolarisation between 23.2 and 15 GHz, but a constant polarisation percentage between 15 and 8.0 GHz. The source rest-frame RM value found for this component of more than $-36,000$

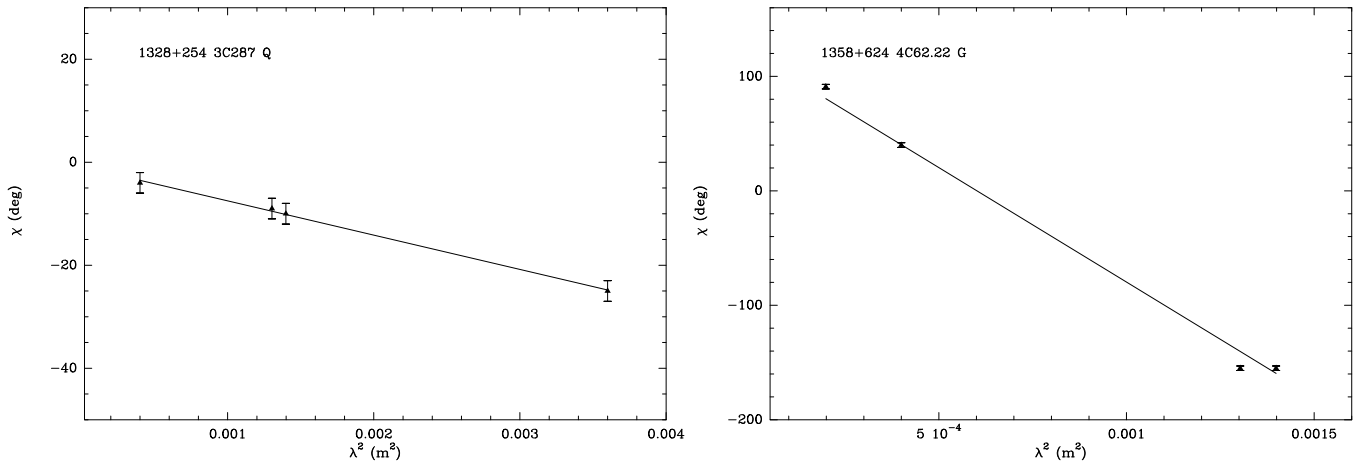


Fig. 2. Plots of the observed χ values of the quasar 1328+254 (3C287) and of the galaxy 1358+624 (4C62.22) as a function of λ^2 for the available frequencies.

rad m⁻² is calculated after adding 180° to χ at 23.3 GHz. Subtracting 180° from χ at 8.0 and 8.4 GHz will generate an even higher RM. Both solutions give acceptable fits to the λ^2 law. If we do not adjust any of the above three χ values, a rare case is implied in which the χ values do not obey the λ^2 law.

The southern component is strongly polarised at 15 GHz, while the polarisation percentage is a factor of 5 lower at X-band. An RM value of RM=5871 rad m⁻² in the source rest-frame can be unambiguously derived.

0319+121 – This source is point-like at 15 GHz, but shows an extension to the north at X-band. VLBI S/X band images from the US Naval Observatory Radio Reference Frame Image Database (<http://rorf.usno.navy.mil/RRFID/>) show a core-jet structure, with the jet in the same direction we find. The source presents little depolarisation from higher to lower frequencies and an RM of zero.

0404+767 (4C76.03) – Again a point-like source at sub-arcsecond resolution. In this case there is a strong depolarisation between 15 and 8.0 GHz. However, the percentage polarisation at 8.4 GHz is much lower than that at 8.0 GHz, which is possibly due to uncertainties caused by the low levels of polarization. Nevertheless, the χ values fit the λ^2 law nicely, with RM=5350 rad m⁻² in the source rest-frame. The VLBI image at 8.0 GHz by Xu et al. (1995) shows a triple structure for 0404+767 at milli-arcsecond resolution.

0531+194 – A compact double source that is unpolarised at the detection levels of all our observations.

0538+498 (3C147) – Our results for this source are fully described in Junor et al. (1999).

0941–080 – A point-like source with polarised emission below the detection limits at all of the available frequencies.

1005–077 (3C237) – The triple structure seen by Lüdke et al. (1998) observing 3C237 with MERLIN at 5 GHz is confirmed by our 15 GHz observations. The central component has a flat spectral index between 5 and 15 GHz, has no detectable polarised emission, and is almost certainly the core of the source. Both lobes are polarised at X- and U-band, showing strong depolarisation between 15 and 8.0 GHz. The lobes are completely depolarised by 5 GHz as reported by Lüdke et al. (1998). The eastern and western lobes have RMs of 942 and 615 rad m⁻² respectively.

3C237 has also been observed by Akujor & Garrington (1995) at 8.4 GHz and by van Breugel et al. (1992) at 15 GHz.

1151–348 – This is a point-like source at sub-arcsecond resolution. It is up to 2.1% polarised at 15 GHz and shows depolarisation towards X-band, with an RM of about zero. Dual-band S/X VLBI observations made by Tzioumis et al. (2002) revealed that 1151–348 has a double structure with the components separated by about 90 milli-arcseconds.

1153+317 (4C31.38) – Our observations at 8 GHz show this to be a double source, with both components being polarised. From the observations of Lonsdale et al. (1993), it is possibly a triple source at 15 GHz. Lonsdale et al. (1993) also observed the source at 5 GHz. Adopting their polarisation measurements, we compute RMs of 913 and 351 rad m⁻² for components **a** and **b** respectively.

1210+134 (4C13.46) – This source presents a very complex structure, dominated by the northern component in which two blobs of emission, both strongly polarised, are embedded in an extended region of weak emission (Fig. 1). A three-arcsecond long jet extends south, beginning from the south-western most of the two blobs mentioned above. Polarised emission is detected all along the jet at X-band. The south-western and north-eastern blobs show RM=640 and -160 rad m⁻² respectively. The values we find for the percentage polarisations are rather puzzling: the brightest component **a** depolarises going from 15 to 8.4 GHz ($DP_{8485/14885} = 0.7$), while component **b** strongly repolarises ($DP_{8485/14885} = 2.3$). Polarised emission is also detected at the three observing frequencies for component **f** at the end of the jet, which also shows repolarisation and has RM=1597 rad m⁻².

1245–197 – This source is slightly resolved at 15 GHz. The image shows an extension to the west of the brightest point-like component. This component is weakly polarised, and has a very large depolarisation index. It is one of the few cases that does not follow the λ^2 law. 1245–197 was also observed with the VLA at 1.36 GHz by Stanghellini et al. (2005) who found a component about 4 arcmin to the west of the main component.

1311+678, 4C67.22 – Polarised emission is not detected for this source which is slightly extended to the south-

east at 15 GHz. 1311+678 shows double structure at milli-arcsecond resolution (see Xu et al. 1995).

1323+321 (4C32.44) – Again a point-like source, it is slightly depolarised between 15 GHz and X-band. However, the percentage polarisation is low. The value of the intrinsic RM is also low ($RM_{rf} = -66 \text{ rad m}^{-2}$). 1323+321 is part of the MOJAVE monitoring programme which is performed with the VLBA at 15 GHz. There it shows a double structure (Lister & Homan 2005) with the two components being separated by about 50 milli-arcsec.

1328+254 (3C287) – This point-like source is about 4% polarised, with little depolarisation from higher to lower frequencies. The intrinsic RM_{rf} is -556 rad m^{-2} . 3C287 was observed by Kellermann et al. (1998) with the VLBA at 15 GHz and showed a point-like structure with a weak extension to the south.

1345+125 (4C12.50) – A point-like source that is only weakly polarised. It presents a very high depolarisation index going from higher to lower frequency and a very large intrinsic RM ($RM_{rf} = -8271 \text{ rad m}^{-2}$). VLBI observations by Stanghellini et al. (1997) at 5 GHz and Kellermann et al. (1998) at 15 GHz reveal a complex, long, thin structure for the source.

1358+624, (4C62.22) – The present observations show a point-like structure for 1358+624. It is weakly polarised, and presents noticeable depolarisation, with a large intrinsic RM ($RM_{rf} = -7496 \text{ rad m}^{-2}$). VLBI observations at 18 cm by Dallacasa et al. (1995) show a double structure with a faint bridge, identified as a jet, connecting the two lobes.

1416+067, (3C298) – This source extends east-west, and is resolved into multiple components. We can identify at least five of these in our 23.2 GHz image, which shows percentage polarisations ranging from about 1% to 7% at 23.2 GHz. Polarised emission was detected only on the eastern side at X-band, while three components show polarisation at 15 GHz. Unexpectedly, components **a** and **b** show repolarisation having $DP_{14885/23285} = 2.6$ and 2.2 respectively, while component **c1** is strongly depolarised ($DP_{14885/23285} = 0.14$). Component **a** is the only one found to be polarised at X-band. It shows depolarization going from 15 to 8.0 GHz.

1416+067 has been the target of many sub- and milli-arcsecond resolution observations. It has been observed by Akujor & Garrington (1995) at 1.6 and 8.4 GHz with the VLA, Lüdke et al. (1998) with MERLIN at 5.0 GHz, and by van Breugel et al. (1992) at 15 GHz with the VLA. We incorporated the values of χ measured for some of the components by these observers to better calculate the RMs. Components **a** and **b** show $RM_{rf} = -883$ and -310 rad m^{-2} , respectively. However, we obtained a much better fit to the λ^2 law for component **b** ($RM_{rf} = -1042 \text{ rad m}^{-2}$) if the χ value at 5.0 GHz of Lüdke et al. (1998) is discarded.

The structure of 3C298 at milli-arcsecond resolution is discussed in depth by Fanti et al. (2002) and references therein. They observed the source with the EVN at wavelengths of 92, 18 and 6 cm.

1458+718 (3C309.1) – The sub-arcsecond structure of 1458+718 is characterised by several components. Three of these are aligned in the east-west direction, while the others lie along the extended emission pointing south, which is clearly detected in both of our X-band images. Polarised emission is detected for the two brightest components, **a** and **b**, at all four of our observing frequencies

3C309.1 has been the target of many other investigations. We mention MERLIN observations at 5 GHz by Lüdke et al. (1998), and by Akujor & Garrington (1995) at 1.4, 5, 8.4, and 15 GHz. The χ values reported by Lüdke et al. (1998), obtained from observations made at comparable resolution, were added to our measurements in order to derive the RMs of three of the components: $RM_{rf} = -3920 \text{ rad m}^{-2}$ for component **a**, $RM_{rf} = 1146 \text{ rad m}^{-2}$ for **a1**, and $RM_{rf} = 10185 \text{ rad m}^{-2}$ for **d**. VLBI images for 3C309.1 can be found in Xu et al. (1995) at 1.6 GHz, and in Kellermann et al. (1998) and Lister & Homan (2005) at 15 GHz. We note that the milli-arcsec images show a north-south core-jet structure, while the source major axis in images at lower resolution is east-west.

1524–136 (OQ172) – We only observed this source at 23.2 GHz since it had already been observed by Mantovani et al. (1994) with the VLA at 6, 4, and 2 cm. It has a double structure, and polarised emission is detected for both of the components at 23.2 GHz. At lower frequencies the polarisation is below the detection limits for the weaker southern component. Combining the observations mentioned here we found the very large RM_{rf} of 20411 rad m^{-2} for the stronger northern component, with virtually no depolarisation from 23.2 to 5.0 GHz.

OQ172 was observed in VLBI by Udomprasert et al. (1997), who find a component close to the source nucleus with an RM_{rf} up to 40000 rad m^{-2} , and by Mantovani et al. (2002), who pointed out that the source is a quasar with a two-sided jet, which is unusual for this class of objects.

1634+628, (3C343) – This source shows a core-jet structure in the VLA images at X-band. The jet (or extension) is not detected at 15 GHz. Polarised emission is detected for the brightest component, showing very little depolarisation and a $RM_{rf} = 2764 \text{ rad m}^{-2}$. Polarimetric VLBA observations at 5 and 8.4 GHz for 3C343 were recently published by Mantovani et al. (2010). Two bright, compact components, surrounded by weak, diffuse emission are detected; both components are polarised. The whole polarised region depolarises little. However, the χ values present large changes, with the RM_{rf} varying across the source, with indications of values higher than 6000 rad m^{-2} .

1638+124 (4C12.60) – The source 1638+124 shows a double structure at the higher of our observing frequencies, appearing slightly resolved at 15 GHz, but point-like at X-band. A value for $RM_{rf} = 14546 \text{ rad m}^{-2}$ is derived for component **a**, which also shows $DP_{14885/23285} = 0.15$.

1641+173 (3C346) – The structure of 3C346 is that of an asymmetric triple source. The western lobe is completely resolved out at 15 and 23.2 GHz. Strong polarised emission (up to 17%) is found for the brightest component of the eastern lobe. This component depolarises quickly with $DP_{14885/23285} = 0.51$, while the RM_{rf} is below 73 rad m^{-2} . This source has also been observed at 1.6, 5, and 8.4 GHz by Akujor & Garrington (1995) at sub-arcsecond resolution, and by Spencer et al. (1991) with MERLIN and EVN at 18 cm, and Cotton et al. (1995) at 1.7 and 8.4 GHz

1829+290 (4C29.56) – This source possesses a triple structure. The central component is the brightest and is polarised at both X-band and 15 GHz, while polarised emission is not detected at 23.2 GHz. Weak polarised emission is also detected for the western lobe at X-band. The two external lobes and the two-sided jet are below the detection

limits at the two higher frequencies. The derived RM_{rf} of 4963 rad m^{-2} is questionable.

1829+290 was observed with the EVN at 1.6 GHz by Dallacasa et al. (1995). Their image shows symmetric, bright, elongated features, likely to be jets, at a position angle of about 90° . This is strongly misaligned with respect to the outer lobes seen on the sub-arcsecond resolution images. The radio core is not detected by Dallacasa et al.

2247+140 (4C14.82) – The 23.2 GHz image of this source shows it to have a double structure. At the lower resolution of X-band, it appears to be point-like, while the double structure can be recognised at 15 GHz. Although, the structure of the polarised emission allowed us to easily separate the two regions, even at the lower resolution, it is difficult to derive the percentage polarisations. It is easier to derive the χ values for the two components, and this has allowed us to calculate $RM_{rf}=319$ and 692 rad m^{-2} .

4. Discussion

4.1. Fractional polarisation

Considering the values of the fractional polarisation listed in Table 1, our VLA A-array observations confirm that CSSs are weakly polarised. However, we find that quasars are more highly polarised than galaxies, and in both cases the polarisation percentages, m , decrease from higher to lower frequencies. This is consistent with a number of earlier results (see e.g. Saikia, Swarup & Kodali 1985; Saikia, Singal & Cornwell 1987; Saikia & Salter 1988, Akujor & Garrington 1995; Cotton et al. 2003a). The differences between galaxies and quasars could be due to a combination of orientation effects and the relative contribution of the jet, which is often more strongly polarized. Point-like sources are the least polarised with a median value of $m \simeq 1\%$. The median m found at X-band confirms the finding by Mantovani et al. (2009) that the median value of m for a complete sample of CSSs observed at the same band was lower than 1%.

The median value of m for individual components in both classes of optical objects decreases slightly going from higher to lower frequencies. However, considering galaxies and quasars separately, we note that the above is confirmed for quasars down to 8085 MHz, while galaxies, in contrast, show strong depolarisation between 14885 and 8085 MHz.

A comparison can be made with the sample of steep spectrum extended radio sources selected from the B3-VLA sample observed at 4.85 GHz by Klein et al. (2003). These authors found a fractional polarisation of 5.2%.

4.2. Rotation Measures

RMs have been calculated for point sources and for many individual components of the sources that are resolved by the VLA A-array. The median values for the modulus $|RM_{rf}|$ are $1146_{-531}^{+2183} \text{ rad m}^{-2}$ for the whole set of source components, $692_{-532}^{+887} \text{ rad m}^{-2}$ for components in quasars, and $1617_{-1298}^{+2135} \text{ rad m}^{-2}$ for components in galaxies. We have 10 galaxies and 6 quasars containing components with RMs higher than the $|RM|$, while 4 galaxies and 13 quasars have RMs lower than this. The dispersion of the RMs is large, ranging from 0 rad m^{-2} to about 36,000 rad m^{-2} in the source rest frame.

A narrower dispersion was found for a sample of 47 CSSs observed with the Effelsberg 100-m telescope by Mantovani et al. (2009). RMs for the 16 sources with polarised emission greater than the detection limits lie between -20 and 3900 rad m^{-2} . This might be expected since sources that are unresolved by single dish observations should show lower levels of polarisation (and RMs) due to the blending of emission from multiple components having different EVPAs. However, among the 12 point-like sources of the present sample, half have RMs close to zero, while 6 show RMs $>500 \text{ rad m}^{-2}$, of which 3 are classified as galaxies.

For comparison, for a sample of faint blazars observed with the Effelsberg 100-m telescope it is found that the RMs range between 0 and 1950 rad m^{-2} . Only 9 out of the 27 objects with polarised emission above the detection limits show $RM >200 \text{ rad m}^{-2}$ (Mantovani et al. (2011).

The lower values of RM for the components in the galaxies compared with quasars is interesting. In the unified scheme this could arise if the quasar components are seen largely through the less dense ionization cones, while the galaxy components may be seen through the torus or the denser interstellar medium of the host galaxy. The errors on the median values are rather large now, and it would be useful to extend such studies to a larger sample of sources. Also although single-dish values have yielded lower values of RM, it is important to study these sources with high resolution to determine their polarimetric properties. A deeper study of the results achieved by this investigation will be given in a future paper.

5. Summary and conclusions

We have presented multi-frequency VLA polarisation observations of CSSs and estimated their percentage polarisations and RM values.

About half of the sources are point-like, even at the $\sim 0.1 \times 0.1$ arcseconds resolution achieved by the present VLA A-array 23.2-GHz observations. The remaining sources have double or triple structures. One source, 1210+134 (4C13.46) shows a complex structure.

Low values for the polarisation percentage in CSSs is confirmed by the present observations. On the average, quasars are more highly polarised than galaxies.

We have compiled the available RM estimates for CSS sources as seen on a sub-arcsecond scale. These show a wide range of values, with indications of very large RMs, although some of the values need to be confirmed via observations at a larger number of frequencies. Values of RM_{rf} as high as $\approx 36\,000 \text{ rad m}^{-2}$ have been found. CSS galaxies are characterized by RM values that are larger than those found for CSS quasars. A majority of the objects show very large values of RM_{rf} .

Acknowledgements. The VLA is operated by the U.S. National Radio Astronomy Observatory, which is a facility of the National Science Foundation operated under a cooperative agreement by Associated Universities, Inc. This research has made use of data from the MOJAVE database that is maintained by the MOJAVE team (Lister et al., 2009). It has also used the NASA/IPAC Extragalactic Database (NED) which is operated by the Jet Propulsion Laboratory, California Institute of Technology, under contract with the National Aeronautics and Space Administration, and NASA's Astrophysics Data System. We regret that it took so long to make these data public. We are very grateful to the referee, Prof. Ralf Spencer, for the very helpful

comments and suggestions he made, and for a careful reading of the manuscript of this paper.

References

- Akujor, C.E., & Garrington, S.T. 1995, *A&AS*, 112, 235
- Cotton, W. D., Feretti, L., Giovannini, G., et al. 1995 *ApJ*, 452, 605
- Cotton, W.D., Dallacasa, D., Fanti, C., et al. 2003b, *A&A*, 406, 43
- Cotton, W.D., Spencer, R.E., Saikia, D.J., & Garrington, S. 2003c, *A&A* 403, 537
- Dallacasa D. and Stanghellini C. 1990, *Proceedings of the workshop Compact Steep-Spectrum & GHz-Peaked Spectrum Radio Sources*, Eds. C. Fanti, R. Fanti, C.P. O’Dea, R.T. Schilizzi
- Dallacasa, D., Fanti, C., Fanti, R., et al. 1995 *A&A*, 295, 27
- Fanti, R., Fanti, C., Schilizzi, R.T. et al. 1990, *A&A* 231, 333
- Fanti, C., Fanti, R., Dallacasa, D. et al. 2002, *A&A*, 396, 801
- Junor, W., Salter, C.J., Saikia, D.J., Mantovani, F., & Peck, A.B. 1999, *MNRAS*, 308, 955
- Klein, U., Mack, K.-H., Gregorini, L. & Vigotti, M. 2003, *A&A*, 406, 579
- Kellermann, K. I., Vermeulen, R. C., Zensus, J. A., & Cohen, M. H. 1998, *AJ*115, 1295
- Lister, M.L., & Homan, D.C. 2005, *AJ*, 130, 1389
- Lister, M. L., Aller, H. D.; Aller, M. F. et al. 2009, *AJ*, 137, 3718
- Lonsdale, C. J., Barthel, P. D., and Miley, G. K., 1993, *ApJS*, 87, 63
- Lüdke, E., Garrington, S.T., Spencer, R.E., et al. 1998, *MNRAS*, 299, 467
- Mantovani, F., Junor, W., Fanti, R. et al. 1994, *A&A*292, 59
- Mantovani, F., Junor, W., Ricci, R., Saikia, D.J., Salter, C., & Bondi, M. 2002, *A&A*, 389, 58
- Mantovani, F., Junor, W., Saikia, D.J., & Salter, C. 2003, *PASA*, 20, 123
- Mantovani, F., Mack, K.-H., Montenegro-Montes, F.M. et al. , 2009, *A&A*, 502, 61
- Mantovani, F., Rossetti, A., Junor, W., et al. 2010, *A&A*, 518, 33
- Mantovani, F., Bondi, M., & Mack, K.-H. 2011, *A&A*, 533, 79
- McCarthy, P.J., Kapahi, V.K., van Breugel W., Persson, S.E., Athreya, R., Subrahmanya, C.R., 1996, *ApJS*, 107, 19
- Nan, R.D., Schilizzi, R.T., Fanti, C. & Fanti, R. 1991, *A&A*, 252, 513
- Saikia, D.J., Swarup, G., & Kodali, P.D. 1985, *MNRAS*, 216, 385
- Saikia, D.J., Singal, A.K., & Cornwell, T.J. 1987 *MNRAS*, 224, 379
- Saikia, D.J., Salter, C.J. 1988, *Annual Review of Astronomy and Astrophysics* Vol. 26, pag. 93
- Sanghera, H.S., Saikia, D.J., Lüdke, E., Spencer, R.E., Foulsham, P.A., Akujor, C.E., Tzioumis, A.K. 1995, *A&A* 295, 629
- Spencer, R.E., Schilizzi, R.T., Fanti, C. et al 1991, *MNRAS*, 250, 225
- Stanghellini, C., O’Dea, C. P., Dallacasa, D., et al. 2005 *A&A*443, 891
- Stanghellini, C., O’Dea, C. P., Baum, et al. 1997 *A&A*325, 943
- Tzioumis, A., King, E., Morganti, R. et al. 2002, *A&A*, 392, 841
- Udomprasert, P. S., Taylor, G. B., Pearson, T. J., & Roberts, D.H. 1997, *ApJ*, 483, L9
- van Breugel, W., Miley, G., & Heckman, T 1984 *AJ*89, 5
- van Breugel, W.J.M., Fanti, C., Fanti, R., et al 1992 *A&A*256, 56
- Xu, W., Readhead, A. C. S., Pearson, T. J., et al. 1995, *ApJS*, 99, 297

Table 1. Percentage polarizations for the whole sample and for galaxies and quasars separately

Frequency MHz	$\langle m_{tot} \rangle$		
	all	G	Q
8085	1.1	0.5	2.8
8485	1.1	0.3	2.8
14885	3.0	1.1	4.2
23285	~ 3.5	~ 2.7	~ 4.0

The table is organised as follows: Column 1: observing frequency; 2-4: the values of the median percentage polarisation $\langle m_{tot} \rangle$ (the ratio of polarised flux density to the total flux density for the whole source) for the sample divided into galaxies (G), and quasars (Q); 5: the median percentage polarisation for the source components considered individually $\langle m_{comp} \rangle$.

Table 2. Integrated polarisation percentages for each source

Name	Other	ID	z	rs	$m_{8.0}$	$m_{8.4}$	$m_{14.8}$	$m_{23.2}$	$DP_{8.0/8.4}$	$DP_{8.4/14.8}$	$DP_{14.8/23.2}$
B0023–263		G	0.3216	D	0.4	0.27	0.67	1.5	1.48	0.40	0.45
B0114–211		G	1.4100	Pe				5.0			
B0116+319	4C31.04	G	0.0602	P	0.27	0.18	–	–	1.50		
B0127+233	3C43	Q	1.4590	T	5.3	5.5	5.2	4.9	0.96	1.06	1.06
B0221+276	3C67	G	0.3102	T	3.3	3.2	3.1		1.03	1.02	
B0223+341	4C34.07	Q	2.9100	D	0.43	0.34	0.58	0.85	1.26	0.59	0.68
B0319+121		Q	2.6620	P	4.4	4.2	4.7		1.05	0.89	
B0404+767	4C76.03	G	0.5985	P	0.2	0.06	3.7		3.3	0.016	
B0531+194		G		D	–	–	–		–	–	
B0538+498	3C147	Q	0.5450	D	0.93	0.98	2.9		0.95	0.34	
B0941–080		G	0.2280	P	–	–	–		–	–	
B1005+077	3C237	G	0.8770	D	0.63	0.73	3.6		0.86	0.2	
B1151–348		Q	0.2580	P	1.3	1.26	2.1		1.03	0.6	
B1153+317	4C31.38	Q	0.4170	D	2.1	2.1			1.0		
B1210+134	4C13.46	Q	1.1389	C	6.6	6.8	6.3		0.97	1.07	
B1245–197		Q	1.2750	Pe	0.07	0.15	0.57		0.47	0.26	
B1311+678	4C67.22	G		P	–	–	–		–	–	
B1323+321	4C32.44	G	0.3680	P	0.78	0.93	1.1		0.84	0.85	
B1328+254	3C287	Q	1.0550	P	4.2	3.9	4.2		1.08	0.93	
B1345+125	4C12.50	G	0.1217	P	0.04	0.15	0.58		0.27	0.26	
B1358+624	4C62.22	G	0.4310	P	0.38	0.24	0.39	–	1.58	0.62	
B1416+067	3C298	Q	1.4373	T	2.6	2.5	3.0	3.2	1.04	0.83	0.94
B1458+718	3C309.1	Q	0.9050	P	5.3	5.3	5.3	5.6	1.0	1.0	0.95
B1524–136		Q	1.6870	D				1.7			
B1634+628	3C343	G	0.9880	P	1.2	1.2	1.3		1.0	0.92	
B1638+124	4C12.60	G	1.1520	P	0.21	0.21	0.63	1.7	1.0	0.33	0.37
B1641+173	3C346	G	0.1620	T	4.4	4.0	3.8	3.6	1.1	1.05	1.06
B1829+290	4C29.56	G	0.8420	T	0.6	0.50	0.8	–	1.20	0.62	
B2247+140	4C14.82	Q	0.2346	P	2.9	3.0	4.5	4.5	0.97	0.67	1.0

The table is organised as follows: Column 1: source name; 2: other name; 3: Optical Identification; 4: Redshift; 5: Radio structure: P point-like, Pe point-like plus extension, D double, T triple, C complex; 6: Polarisation percentage at 8085 MHz; 7: Polarisation percentage at 8485 MHz; 8: Polarisation percentage at 14885 MHz; 9: Polarisation percentage at 23285 MHz; 10: Depolarisation index, DP, between 8485 and 8085 MHz; 11: Depolarisation index, DP, between 14885 and 8485 MHz; 12: Depolarisation index, DP, between 23285 and 14885 MHz.

Table 3. Polarisation parameters for components of each source at 8085 MHz

Name	Other name	ID	comp	S mJy	3σ mJy/b	S_p mJy	$3\sigma_p$ mJy/b	χ deg	maj arcsec	min arcsec	PA deg
B0023–263		G	a	1329.2	0.29	5.7	0.15	53	0.16	0.05	158
			b	848.2		3.3		49	0.11	0.06	129
B0116+319	4C31.04	G		1097.8	0.22	3.0	0.11	–4	0.10	0.02	116
B0127+233	3C43	Q	a ₁₂	637.2	0.21	12.8/16.0	0.12	80/13	0.21	0.11	148
			b	114.6		10.7		–33	1.1	0.2	59
			c	24.6		1.4		44	0.33	0.26	139
B0221+276	3C67	G	a	228.8	0.08	19.6	0.09	50–80	0.58	0.19	173
			b	357.4					0.17	0.13	176
B0223+341	4C34.07	Q	a	1254.0	0.18	4.6	0.12	–6	0.03	0.02	43
			b	66.2		1.1		–54	0.22	0.07	81
B0319+121				1228.1	0.15	54.0	0.10	67	0.03	0.003	158
B0404+767	4C76.03	E		2194.9	0.27	4.4	0.14	–41	0.076	0.013	43
B0531+194		G	a	703.7	0.15		0.09		0.19	0.09	139
			b	751.3					0.23	0.09	123
B0538+498	3C147	Q	a	4474.6	0.36	32.2	0.10	–23	0.33	0.26	57
			b	393.6		12.5		–70	0.32	0.27	24
B0941–080		G		706.0	0.12		0.09		0.046	0.01	144
B1005+077	3C237	G	a	684.7	0.12	6.5	0.09	28	0.16	0.06	78
			b	462.6		0.7		–52	0.15	0.06	87
B1151–348		Q		1749.8	0.21	22.7	0.31	20	0.11	0.05	60
B1153+317	4C31.38	Q	a	400.0	0.08	3.4	0.09	–62	0.11	0.06	8
			b	214.9		9.7		22	0.11	0.04	48
B1210+134	4C13.46	Q	a	307.5	0.08	22.0	0.09	45	0.15	0.09	15
			b	200.0		8.4		33	0.21	0.13	135
			c	1.8					0.68	0.19	125
			d	8.8		1.8		55	0.28	0.22	165
			e	6.5		0.2		–42	0.65	0.35	1
			f	15.3		3.3		–84/–57	0.48	0.21	134
B1245–197		Q		1553.2	0.21	0.07	0.14	58	0.09	0.02	87
B1311+678	4C67.22	E		608.1	0.06		0.09		0.06	0.02	112
B1323+321	4C32.44	G		1620.9	0.20	12.6	0.09	7	0.06	0.01	134
B1328+254	3C287	Q		2239.6	0.30	92.9	0.10	–10	0.06	0.04	25
B1345+125	4C12.50	G		2291.7	0.40	1.0	0.10	42	0.06	0.015	170
B1358+624	4C62.22	G		1182.9	0.05	4.5	0.18	25	0.03	0.01	124
B1416+067	3C298	Q	a+b	304.1	0.08	12.1/11.0	0.12	–55/–7	0.25	0.12	85
			c	215.2					0.03	0.0	46
			d	388.7					0.69	0.13	102
			e	32.1		0.8		–44	0.63	0.39	162
B1458+718	3C309.1	Q	a/a ₁	359.9	0.33	15.4/11.8	0.15	–70/–16	0.41	0.18	116
			b	1598.0		80.2		49	0.087	0.044	76
			c	26.4		0.6		78	0.45	0.27	67
			d	83.3		1.5		–48	0.36	0.29	99
			e	32.1		0.8		–44	0.63	0.39	162
B1634+628	3C343	G	a	825.3	0.14	9.9	0.10	80	0.09	0.06	94
			b	5.4					0.79	0.28	59
B1638+124	4C12.60	E		788.1	0.13	1.72	0.09	–77	0.14	0.012	130
B1641+173	3C346	G	a ₁₂₃	331.4	0.10	0.7/17.3/7.6	0.09	0/–36/1	–	–	–
			b	205.3					0.015	0.0	1
			c	40.7					3.11	0.9	54
B1829+290	4C29.56	G	a	11.4	0.10		0.10		0.62	0.22	88
			c+b	685.1		4.2		–28	0.077	0.014	86
			d	2.2					0.40	0.04	62
			e	10.3		0.3		–45	0.61	0.27	56
			a+b	833.1	0.21	17.1/7.1	0.12	–78/15	0.21	0.07	31

The table is organised as follows: Column 1: source name; 2: other name; 3: Optical Identification; 4: component; 5: integrated component flux density; 6: three σ noise in total-intensity image; 7: polarised flux density; 8: three σ noise in the polarised-intensity density; 9: EVPA; 10-12: deconvolved sizes of the components; major axis, minor axis, and position angle of the major axis, respectively.

Table 4. Polarisation parameters for components of each source at 8485 MHz

Name	Other name	ID	comp	S mJy	3σ mJy/b	S_p mJy	$3\sigma p$ mJy/b	χ deg	maj arcsec	min arcsec	PA deg
B0023–263		G	a	1261.8	0.30	3.8	0.15	63	0.16	0.05	157
			b	893.7		2.0		59	0.12	0.06	133
B0116+319	4C31.04	G		1070.8	0.30	1.97	0.10	–4	0.09	0.019	116
B0127+233	3C43	Q	a12	619.2	0.11	6.4/20.7	0.11	80/13	0.21	0.11	147
			b	98.4		11.9		–34	1.0	0.18	58
			c	25.5		1.9		44	0.43	0.29	136
B0221+276	3C67	G	a	219.0	0.07	17.8	0.08	50–80	0.58	0.18	173
			b	339.6					0.16	0.13	175
B0223+341	4C34.07	Q	a	1225.6	0.11	3.6	0.09	–4	0.03	0.014	54
			b	55.2		0.8		–55	0.019	0.085	77
B0319+121				1211.8	0.15	50.9	0.12	67	0.03	0.002	160
B0404+767	4C76.03	E		2124.2	0.16	1.26	0.13	–60	0.076	0.007	43
B0531+194		G	a	624.3	0.15	0.8	0.08	–45	0.23	0.09	136
			b	719.3		0.4		–45	0.21	0.09	122
B0538+498	3C147	Q	a	4258.0	0.39	31.6	0.15	–18	0.22	0.06	55
			b	370.3		13.6		–75	0.40	0.10	18
B0941–080		G		673.5	0.12		0.11		0.06	0.009	142
B1005+077	3C237	G	a	659.9	0.12	6.9	0.09	34	0.16	0.06	78
			b	439.0		1.1		–52	0.16	0.07	88
B1151–348		Q		1678.7	0.81	21.0	0.39	26	0.11	0.04	60
B1153+317	4C31.38	Q	a	383.1	0.06	2.6	0.08	–66	0.10	0.06	5
			b	203.3		9.6		22	0.10	0.04	48
B1210+134	4C13.46	Q	a	297.4	0.07	20.7	0.11	49	0.15	0.10	11
			b	177.4		8.1		34	0.20	0.12	112
			c	10.2				–	–	–	–
			d	10.1		2.1		62	0.33	0.27	2
			e	3.9		0.3		–46	0.45	0.35	176
			f	14.7		3.7		–84/–57	0.57	0.24	143
B1245–197		Q		1486.7	0.17	2.2	0.13	–76	0.088	0.016	87
B1311+678	4C67.22	E		583.1	0.10		0.08		0.06	0.02	113
B1323+321	4C32.44	G		1566.8	0.21	14.6	0.11	15	0.06	0.013	133
B1328+254	3C287	Q		2167.2	0.33	85.4	0.19	–9	0.064	0.039	23
B1345+125	4C12.50	G		2215.9	0.51	3.3	0.11	–81	0.063	0.013	170
B1358+624	4C62.22	G		1136.5	0.14	2.7	0.12	25	0.036	0.007	119
B1416+067	3C298	Q	a+b	286.0	0.09	11.3/10.4	0.07	–57/–6	0.25	0.12	85
			c	210.4					0.04	0.0	47
			d	357.2					0.68	0.14	103
B1458+718	3C309.1	Q	a/a1	348.0	0.28	14.1/11.4	0.15	–64/–18	0.42	0.18	116
			b	1543.1		78.0		49	0.080	0.044	78
			c	28.7				78	0.53	0.33	172
			d	75.9		1.6		–48	0.36	0.24	96
			e	41.4				–44	1.00	0.54	28
B1634+628	3C343	G	a	778.1	0.16	9.1	0.09	77	0.083	0.062	100
			b	3.3					0.62	0.33	123
B1638+124	4C12.60	E		757.0	0.10	1.60	0.08	–77	0.14	0.02	130
B1641+173	3C346	G	a123	311.6	0.06	0.0/15.5/7.6	0.07	–/–36/0	–	–	–
			b	206.7					0.007	0.00	37
			c	43.6					1.41	0.82	95
B1829+290	4C29.56	G	a	9.2	0.07		0.09		0.45	0.22	87
			c+b	652.5		3.2		–30	0.07	0.010	87
			d	1.6					0.28	0.09	49
			e	11.0		0.2		–45	0.58	0.52	28
B2247+140	4C14.82	Q	a+b	794.9	0.36	17.2/6.8	0.08	–79/15	0.21	0.05	31

The table is organised as follows: Column 1: source name; 2: other name; 3: Optical Identification; 4: component; 5: integrated flux density of the components; 6: three σ error on the total-intensity image; 7: polarised flux density; 8: three σ error on the polarised-intensity image; 9: EVPA; 10-12: deconvolved sizes of the components; major axis, minor axis, and position angle of the major axis, respectively.

Table 5. Polarisation parameters for components of each source at 14885 MHz

Name	Other name	ID	comp	S mJy	3σ mJy/b	S_p mJy	$3\sigma_p$ mJy/b	χ deg	maj arcsec	min arcsec	PA deg
B0023–263		G	a12	747.70	0.54	2.9/2.1	0.45	45/–14	0.11	0.03	150
			b	509.30		3.4		–23	0.089	0.038	129
B0116+319	4C31.04	G		746.30	0.33		0.38		0.098	0.025	114
B0127+233	3C43	Q	a1	241.80	0.30	11.4	0.34	14	0.13	0.05	86
			a2	162.00		11.7		81	0.12	0.0	2
			b	27.90					0.53	0.16	55
			c	8.48					0.28	0.07	37
B0221+276	3C67	G	a12	100.7	0.21	5.4	0.23	25	0.61	0.164	172
			a3	8.6					–	–	–
			b	178.0		3.6		–49	0.14	0.12	168
			c	1.24					0.06	0.026	168
B0223+341	4C34.07	Q	a	845.40	0.21	3.2	0.30	–70	0.017	0.006	108
			b	25.7		1.9		–75	0.158	0.055	88
			b0	3.38					0.25	0.04	59
B0319+121				934.80	0.27	43.6	0.28	67	0.018	0.005	164
B0404+767	4C76.03	E		1496.00	0.27	54.7	0.32	25	0.06	0.010	46
B0531+194		G	a	294.20	0.33		0.30		0.124	0.084	138
			b	365.90					0.15	0.077	123
B0538+498	3C147	Q	a1	1409.70	0.42	58.1	0.42	50	0.06	0.0	105
			a2	1029.40		2.9		45	0.12	0.06	63
			b	178.10		15.1		90	0.21	0.08	16
B0941–080		G		390.40	0.24				0.065	0.008	143
B1005+077	3C237	G	a	336.20	0.18	15.9	0.30	2/42	0.16	0.04	78
			b	215.00		4.0		0	0.12	0.05	85
			b1	3.86					0.14	0.04	105
B1151–348		Q		966.40	0.68	20.0	0.64	9	0.10	0.04	68
B1210+134	4C13.46	Q	a	205.8	0.18	20.2	0.30	40	0.08	0.05	42
			b	116.3		2.3		35	0.04	0.03	21
			c	26.4?					–	–	–
			d	3.20					0.49	0.23	137
			f	5.30					0.40	0.15	141
B1245–197		Q	a	804.9	0.24	5.0	0.32	52	0.0	0.0	102
			b	71.8					0.11	0.02	102
B1311+678	4C67.22	E		328.30	0.15		0.32		0.05	0.02	113
B1323+321	4C32.44	G		1038.00	0.27	11.4	0.19	11	0.06	0.010	132
B1328+254	3C287	Q		1389.0	0.42	58.8	0.25	–4	0.05	0.03	28
B1345+125	4C12.50	G		1535.0	0.18	8.9	0.25	20	0.06	0.01	171
B1358+624	4C62.22	G		721.04	0.45	2.8	0.32	45	0.029	0.011	96
B1416+067	3C298	Q	a	85.40	0.25	6.1	0.32	–63	0.12	0.07	33
			b	46.3		6.1		–2	0.19	0.07	71
			c1	70.50		0.7		–1	0.11	0.03	96
			c2	167.20					0.014	0.0	54
			d	60.10					0.08	0.07	41
			a	76.60	0.36	7.7	0.43	–87/–46	0.16	0.0	13
B1458+718	3C309.1	Q	a0	104.7					0.39	0.21	110
			a1	38.3		3.3		–23	0.022	0.096	95
			b	1051.90		58.2		45	0.048	0.025	146
			d	28.00					0.28	0.15	89
B1634+628	3C343	G	a	376.00	0.18	5.1	0.32	42	0.07	0.05	87
B1638+124	4C12.60	E	a	432.10	0.23	0.7	0.30	–1	0.02	0.01	122
			b	91.90		2.6		90	0.04	0.02	172
B1641+173	3C346	G	a12	171.30	0.15	1.2/14.0	0.34	–35	0.14	0.08	95
			a3	10.20		1.2		–1	0.18	0.09	115
			b	239.70					0.005	0.003	133
B1829+290	4C29.56	G	a	–	0.24		0.30		–	–	–
			c	356.70		2.9		52	0.06	0.01	86
			c1	2.60					0.20	0.02	51
			d	–					–	–	–
B2247+140	4C14.82	Q	a	376.30	0.24	18.5	0.32	–85	0.07	0.03	63
			b	207.40		7.9		13	0.13	0.06	162

The table is organised as follows: Column 1: source name; 2: other name; 3: optical identification; 4: component; 5: integrated flux density of the components; 6: three σ error on the total-intensity image; 7: polarised flux density; 8: three σ error on the polarised-intensity image; 9: EVPA; 10–12: deconvolved sizes of the components; major axis, minor axis, and position angle of the major axis, respectively.

Table 6. Polarisation parameters for the components of each source at 23285 MHz

name	other name	ID	comp	S mJy	3σ mJy/b	S_p mJy	$3\sigma_p$ mJy/b	χ deg	maj arcsec	min arcsec	PA deg
B0023–263		G	a12	489.3	0.42	3.2	0.70	43	0.07	0.01	152
			b	316.8		8.6		34	0.06	0.03	131
B0114–211		G		141.3	0.27	7.1	0.47	1	0.054	0.019	112
B0116+319	4C31.04	G		550.2	0.27		0.30		0.10	0.026	112
B0127+233	3C43	Q	a1	113.0	0.24	5.0	0.28	3	0.14	0.02	178
			a2	79.2		5.6		48	0.08	0.05	124
B0223+341	4C34.07	Q	b	25.7					–	–	–
			a	610.2	0.21	5.3	0.36	1	0.05	0.005	114
			b	12.4						0.126	0.052
B1358+624	4C62.22	G	b0	3.1					0.09	0.09	51
			a	486.0	0.30		0.43		0.03	0.003	118
B1416+067	3C298	Q	a	36.8	0.24	1.0	0.36	–70	0.13	0.08	65
			b	16.1		0.96		1	0.16	0.06	81
			c1	42.1		3.0		23	0.16	0.03	114
			c2	83.3		0.8		73/37	0.04	0.008	118
			d	18.9		0.4		–88	0.09	0.06	85
B1458+718	3C309.1	Q	a	92.1	0.48	5.4	0.43	90/–25	0.19	0.16	161
			a0						–	–	–
			a1	26.5		2.6		–35	0.023	0.08	93
			b	767.6		41.9		46	0.048	0.020	151
			d	11.8					0.23	0.12	92
B1524–136		Q	a	279.0	0.30	4.9	0.47	65	0.10	0.012	163
			b	35.3		0.6		88	0.06	0.05	74
B1638+124	4C12.60	E	a	304.4	0.21	3.3	0.36	81	0.0	0.0	0
			b	56.5		2.8		76	0.06	0.02	142
B1641+173	3C346	G	a12	79.8	0.30	1.3/10.4	0.38	–43	0.12	0.07	85
			a3	5.1		1.3		–1	0.12	0.08	163
			b	234.2					0.003	0.0	106
			c	43.6					1.41	0.82	95
B1829+290	4C29.56	G	c	182.1				0.059	0.008	87	
B2247+140	4C14.82	Q	a	257.5	0.18	14.8	0.32	60/–76	0.074	0.024	56
			b	159.5		3.8		14	0.21	0.06	17

The table is organised as follows: Column 1: source name; 2: other name; 3: optical identification; 4: component; 5: flux density; 6: three σ error on the total-intensity image; 7: polarised flux density; 8: three σ error on the polarised-intensity image; 9: EVPA; 10-12: deconvolved sizes of the components; major axis, minor axis, and position angle of the major axis, respectively.

Table 7. Fractional polarisation, depolarisation index and Rotation Measure for individual components of each source.

name	other name	ID	comp	$m_{8.0}$ [%]	$m_{8.4}$ [%]	$m_{14.8}$ [%]	$m_{23.2}$ [%]	$DP_{8.0/8.4}$	$DP_{8.4/14.8}$	$DP_{14.8/23.2}$	RM rad m ⁻²	RM _{rf} rad m ⁻²	
B0023–263		G	a	0.43	0.30	0.67	0.65	1.43	0.45	1.03	146	255	
			b	0.39	0.22	0.67	2.71	1.64	0.33	0.25			
B0114–211		G					5.02				646	3752	
B0116+319	4C31.04	G		0.27	0.18			1.50					
B0127+233	3C43	Q	a1	4.52	4.38	4.71	4.1	1.03	0.93	1.67	-24	-145	
			a2			7.22	7.07			1.02		-23	-139
			b	9.34	12.09				0.72				
B0221+276	3C67	G	a1	8.57	8.13	5.36		1.05	1.51		768	1318	
			a2									942	1617
			b			2.02						1745	2995
B0223+341	4C34.07	Q	a	0.37	0.29	0.38	0.87	1.28	0.76	0.44	-2373	-36279	
			b	1.66	1.45	7.39		1.14	0.20			384	5871
B0319+121				4.40	4.20	4.66		1.05	0.90		0	0	
B0404+767	4C76.03	E		0.20	0.06	3.66		3.33	0.02		2090	5350	
B0531+194		G	a		0.13								
			b		0.06								
B0538+498	3C147	Q	a1	0.72	0.74	4.12		0.97	0.18				
			a2			0.28							
			b	3.18	3.67	8.48		0.87	0.43				
B1005+077	3C237	G	a	0.95	1.05	4.73		0.90	0.22		-174	-615	
			b	0.15	0.25	1.86		0.60	0.13			-942	-3329
B1151–348		Q		1.3	1.25	2.1		1.04	0.60		0	0	
B1153+317	4C31.38	Q	a	0.85	0.68			1.25			453	913	
			b	4.51	4.72			0.96				174	351
B1210+134	4C13.46	Q	a	7.15	7.00	9.82		1.02	0.71		140	640	
			b	4.20	4.60	1.98		0.91	2.32			-35	-160
			d	20.45	20.79			0.98					
			e	3.08	7.69			0.40					
			f	21.57	25.17	17.0		0.86	1.48			349	1597
			a	0.07	0.15	0.62		0.47	0.24				
B1245–197		Q		0.78	0.93	1.10		0.84	0.85		-35	-66	
B1323+321	4C32.44	G		4.15	3.94	4.23		1.05	0.93		-131	-556	
B1328+254	3C287	Q		0.04	0.15	0.58		0.27	0.26		-5585	-8271	
B1358+624	4C62.22	G		0.38	0.24	0.39		1.58	0.61		-3665	-7496	
B1416+067	3C298	Q	a	7.60	7.59	7.14	2.72	1.00	1.06	2.63	-140	-833	
			b			13.17	5.96			2.21		-175	-1042
			c1			0.99	7.13			0.14			
			c2				0.96						
			d				2.12						
B1458+718	3C309.1	Q	a	7.56	7.33	10.05	5.86	1.03	0.73	1.71	-1047	-3920	
			a1			8.62	9.81			0.88		314	1146
			b	5.02	5.05	5.53	5.46	0.99	0.91	1.01			
			c	2.27									
			d	1.80	2.11	1.8		0.85				2792	10185
e	2.49												
B1524–136	OQ172	Q	a				1.76				2827	20411	
			b				1.70						
B1634+628	3C343	G	a	1.20	1.17	1.36		1.03	0.86		698	2764	
B1638+124	4C12.60	E	a	0.22	0.21	0.16	1.08	1.05	1.31	0.15	3141	14546	
			b			2.83	4.96			0.57			
B1641+173	3C346	G	a12	7.72	7.41	8.87	14.66	1.04	0.84	0.60	54	73	
			a3			11.76	25.49			0.46		17	23
B1829+290	4C29.56	G	c	0.61	0.49	0.81		1.24	0.60		-1466	-4963	
			e	2.91	1.82			1.60					
B2247+140	4C14.82	Q	a	2.90	3.02	4.92	5.75	0.96	0.61	0.85	209	319	
			b			3.81	2.38			1.60		454	692

The table is organised as follows: Column 1: source name; 2: other name; 3: optical identification; 4: component; 5: percentage of polarised emission at 8085 MHz; 6: percentage of polarised emission at 8485 MHz; 7: percentage of polarised emission at 14885 MHz; 8: percentage of polarised emission at 23285 MHz; 9: depolarisation index between 8485 MHz and 8085 MHz; 10: depolarisation index between 14885 MHz and 8485 MHz; 11: depolarisation index between 23285 MHz and 14885 MHz; 12: Rotation Measure; 13: Rotation Measure in the source rest frame $RM_{rf}=RM \times (1+z)^2$.